Understanding the diurnal cycle of land-atmosphere interactions from flux site observations

Eunkyo Seo[1], Paul A. Dirmeyer[1]

[1] Center for Ocean-Land-Atmosphere Studies, George Mason University, Fairfax, 22030, United States

5 *Correspondence to*: Eunkyo Seo (eseo8@gmu.edu)

Abstract. Land–atmosphere interactions have been investigated at daily or longer time scales due to limited data availability and large sensor errors for measuring high-frequency signals. Yet coupling at the sub-daily time scale is characterized by the diurnal cycle of incoming solar radiation and soil wetness. Based on flux tower observations, this study investigates the climatology of the observed land–atmosphere interactions on a sub-daily time scale during the warm season. Process-based
10 multivariate metrics are employed to quantitatively measure the segmented coupling processes and the mixing diagram is adopted to demonstrate the integrative moist and thermal energy budget evolution in the atmospheric mixed layer. The land, atmosphere, and combined couplings for the entire daily mean, midday, and midnight show the different situations to which surface latent and sensible heat fluxes are relevant, and they also reveal the climate sensitivity to soil moisture and surface air temperature. The coevolution of the diurnal moisture and thermal energy within the boundary layer traces a particular path on
15 mixing diagrams, exhibiting different degrees of hysteresis in water– and energy–limited locations. Water– and energy–limited processes also show opposing long tails during the daytime and night-time related to the impact on the land and atmospheric couplings via latent heat flux and other diabatic processes like radiative cooling. This study illustrates the necessity of considering the whole diurnal cycle to understand land-atmosphere coupling processes comprehensively in observations and modelling.

20 ## 1 Introduction

Land–atmosphere (L–A) interactions play a critical role in the global energy and water cycles. Our understanding of L–A interactions has increased greatly over the last 20 years, initially via numerous climate modelling studies. These have included several multi-model experiments (Koster et al., 2011, 2002; Dirmeyer et al., 2006; Seneviratne et al., 2013; Lawrence et al., 2016; Van Den Hurk et al., 2016; Xue et al., 2016, 2021), and single model studies too numerous to mention. Among the most
25 important multi-model studies was the Global Land–Atmosphere Coupling Experiment (GLACE), which focused on how land surface states (namely soil moisture) can affect atmospheric processes (Koster et al., 2004, 2006; Guo et al., 2006), leading to the identification of hotspot locations of L–A coupling.

In recent years, the growing availability of observational data (both *in situ* measurements and satellite retrievals) has made possible a new wave of studies that is enhancing our understanding of L–A interactions and enabling more thorough

30 evaluations of model performance. Growing *in situ* monitoring networks of soil moisture are enabling new evaluation capabilities (Dorigo et al., 2011; Quiring et al., 2016; Dirmeyer et al., 2016). Flux towers have reached a level of quality, coverage and longevity that make them invaluable to studies of L–A interactions (Novick et al., 2018; Tramontana et al., 2016). Satellites are providing ever improving coverage and quality of land surface states, and increasingly fluxes (Miralles et al., 2016; Alemohammad et al., 2017; Colliander et al., 2017; Dorigo et al., 2017; Ma et al., 2019; Seo and Dirmeyer, 2022).

35 Tawfik et al. (2015b) demonstrated linkages between land surface fluxes and convective initiation from radiosonde data. Denissen et al. (2021) found soil moisture signals globally in boundary layer profiles. Zhang et al. (2020) have applied sounding data from commercial aircraft to quantify land surface drivers of boundary layer development. Dirmeyer et al. (2018) verified L–A coupling in forecast models, reanalyses, and land surface models against *in situ* observations using process-based multivariate statistics, demonstrating that the models generally underrepresent spatial and temporal variability relative to

40 observations. Wulfmeyer et al. (2018) are developing a new generation of surface and lower atmosphere monitoring capabilities that will provide unprecedented data on local L–A interactions. Data assimilation and other synthesis techniques can extend the data coverage while compensating for both model and sensor errors (Crow et al., 2015; Reichle et al., 2017; Seo et al., 2021).

Moreover, the increased data availability of hydrological and near-surface atmospheric variables can be used to improve

45 understanding of L–A interactions following links in the process chains described by Santanello et al. (2018). The linkages begin with soil moisture and its controls on surface heat flux partitioning, its effects on soil heat storage, conduction, and the health of vegetation. This process chain strongly influences on the L–A feedbacks in the development of extreme climate events (e.g., heat wave and drought) (Seneviratne et al., 2010; Miralles et al., 2012, 2019; Schumacher et al., 2019; Seo et al., 2020; Dirmeyer et al., 2021). The coupling is not necessarily linear, and the soil moisture–evaporation relationship has been

50 strengthened when the soil moisture and temperature become drier and warmer, respectively, which emphasizes anomalous warming and drying to the extreme (Benson and Dirmeyer, 2021). Thus, the realistic representation of L–A coupling in a subseasonal-to-seasonal forecast system is a key to improved prediction skill (Seo et al., 2019; Koster et al., 2011).

Most L–A coupling metrics (refer to Table 1 in Santanello et al. (2018)) have focused on daily mean conditions, using data commonly available from models when L-A interaction studies began. However, some metrics use information at specific

55 times of day to focus on time-evolving processes within the diurnal cycle. For instance, the mixing diagram, an integrative diagnostic metric of the L–A coupling process chain, demonstrates the daytime coevolution of energy and water budgets within the mixed layer (ML) (Santanello et al., 2009, 2011). This synthesized metric can be decomposed into land and atmospheric components that are further explained by linked moist and thermal processes to quantify interactions and feedbacks across a range of scales. The convective triggering potential (CTP) and low-level humidity index (HI_{low}) characterize the circumstances

60 in which the L–A coupling could influence afternoon convection (Findell and Eltahir, 2003b, a). It is based on the concept that morning atmospheric profiles of temperature and humidity can provide information on whether boundary layer conditions are favourable to trigger convection during the day. Findell et al. (2011) established that morning evaporation increases lead to an enhanced probability of afternoon rainfall over much of the United States, whereas rainfall intensity appears insensitive to

surface fluxes. The heated condensation framework (HCF) also examines the impact of surface fluxes on convective triggering later in the day based on a synthetic evolution of atmospheric profiles of temperature and humidity based on idealized surface fluxes (Tawfik and Dirmeyer, 2014; Tawfik et al., 2015a). The probability of convective initiation was found to be more sensitive to morning convective inhibition over the southeastern United States, and soil moisture provides a secondary control on convection (Tawfik et al., 2015b).

Nevertheless, thorough examinations of the complete diurnal cycle of L–A interactions have been lacking. A major barrier has been the availability of reliable data that resolves the diurnal cycle, particularly for soil moisture. Although dielectric sensors are extensively used in soil moisture monitoring networks, their diurnal cycle at shallow soil depths tends to include a spurious component due to their high temperature sensitivity, causing a positive measurement bias that peaks during the time of maximum soil temperature (Kapilaratne and Lu, 2017). To date, there is no adequate temperature correction method for dielectric sensors, so typically hourly or sub-hourly measurements are averaged to daily means, or measurements at a single hour of the day are used, to avoid the sensor problem. Although cosmic ray neutron sensors do not have this problem (Zreda et al., 2008; Evans et al., 2016), the cosmic sensor has a variable measurement footprint and depth, and is not as widely used due to its expense. Polar orbiting satellites also avoid this problem with sun-synchronous overpasses near sunrise and sunset, providing data at the same hour of the day (Entekhabi et al., 2010; Kerr et al., 2010). However, they do not sample the entire diurnal cycle, at best providing measurements twice per day at any location, and depending on latitude, may only pass over a location every few days.

By taking into account the issues included in diverse observational datasets, the investigation of the complete diurnal cycle of the observed L–A interactions can begin to understand the comprehensive L–A coupling processes. In this study, we examine the entire diurnal cycle of the climatological L–A interactions at available flux tower sites across the globe for the hemispheric warm season. The terrestrial coupling index is adopted to explore the L–A coupling process chain and the mixing diagram is employed to synthesize the coevolution of moist and thermal energy budget within the ML. We sidestep the soil moisture problem by grouping data by each hour of the day and calculate correlation-based daily coupling metrics independently at each hour. In so doing, new details of the daily evolution of L–A coupling are revealed. Section 2 introduces the datasets used in this study. Section 3 describes the adopted metrics to understand the L–A interactions, and our composition approach to investigate the climate sensitivity. Section 4 presents and discusses the results of this study. Finally, section 5 summarizes the results and their implications for future applications.

2 Data

2.1 Flux site observations

In situ measurements of near-surface meteorological variables, land surface heat fluxes, and surface soil moisture are employed to understand L–A interactions on sub-diurnal time scales. The FLUXNET2015 station dataset version released in February

2020 has collected data from multiple regional flux networks across the globe spanning 1996–2020 (https://fluxnet.org/data/fluxnet2015-dataset/; (Pastorello et al., 2020). The tier 1 data is used in this study, additionally screened by the quality flag for each variable marked 0 or 1 (0: measured and 1: good quality gap-filled value following the method of Reichstein et al. (2005)). In addition, if the IGBP classification of any sites is snow and ice (IGBP classification is

100 "SNO"), the sites are discarded. To extend the observational flux data across more stations and into more recent years, this study also uses data from the AmeriFlux network (https://ameriflux.lbl.gov/) and the European Drought-2018 network (https://doi.org/10.18160/YVR0-4898). Data from these additional sources are available in a format that matches the FLUXNET2015 standards. To examine the diurnal L–A interactions, this study uses half-hourly or hourly data from all three network datasets and composites all sites to hourly intervals. Where FLUXNET2015 spatially and temporally overlaps the

105 AmeriFlux or European Fluxes Database station data, the FLUXNET2015 is given priority and the other datasets are used to extend the temporal coverage of the FLUXNET2015 data. Fig. 1 shows the global distribution of sites along with their land cover categories. 230 sites are available, but the spatial coverage is concentrated in a few midlatitude regions, especially over North America, Europe, and Australia. The adopted variables in this study are soil wetness content in the top soil layer (SWC1), sensible (H) and latent heat fluxes (LE), surface air temperature, humidity, surface pressure, and vapor pressure. To understand

110 the atmospheric coupling processes related to land surface heat fluxes, we calculate the lifted condensation level (LCL) using the variables measured at each site:

$$LCL = \frac{T - T_d}{\Gamma_d - \Gamma_{dew}} \tag{1}$$

where T and T_d are surface air temperature and dew-point temperature, respectively. The terms of Γ_d and Γ_{dew} are the lapse rate for dry adiabatic lifting (9.8×10^{-3} K/m), and the lapse rate of the dew point (1.8×10^{-3} K/m), respectively. LCL is reported

115 in units of meters.

2.2 ERA5 reanalysis

Information on planetary boundary layer (PBL) height (Z_{PBL}) is needed in the mixing diagram approach described in section 3.3, in order to estimate the temperature and humidity budgets in the ML, but flux tower sites do not typically measure PBL

120 height. This study alternatively adopts Z_{PBL} from the European Centre for Medium-Range Weather Forecasts (ECMWF) Reanalysis version 5 (ERA5; Hersbach et al., 2020) on the model's native grid, corresponding to a horizontal spatial resolution of ~31 km and an hourly temporal resolution. Z_{PBL} from the ERA5 grid cell containing each flux site location is associated with that location. Although there are some issues to bring the gridded data to the observed site due to unresolved spatial heterogeneity in ERA5, this study assumes that the mesoscale variability of Z_{PBL} is small compared to its temporal variability.

125

3 Methodology

3.1 Data pre-processing

Coupling metrics are calculated separately for each month to remove the seasonal cycle, and then monthly statistics are averaged for each hemisphere's warm season (NH: May–September, SH: November–March) to focus on the most active
130 season for L–A coupling. However, it should be noted that the temporal data coverage for each flux site varies greatly; some stations have more than two decades of data, others only a few years. Moreover, to avoid the confounding effects of precipitation on correlation-based metrics, substantial rainfall days are identified when daily soil moisture tendencies are positive and larger than 2-standard deviations; those days are removed from the calculations. Only when all 24-hourly values are available for a given day are they included in the analysis.

135 ### 3.2 Terrestrial coupling index

To quantify L–A interactions, this study uses the terrestrial coupling index, proposed by Dirmeyer (2011), to characterize the sensitivity of the target variable (i.e., land surface fluxes) to the representative variability of the source variable (i.e., soil moisture). It is formulated as:

$$TCI_h(SV_h, TV_h) = R(SV_h, TV_h) \times SD(TV_h) \qquad (2)$$

where SV and TV are the source and target variables, respectively, and the subscript h refers to the local hour of the day. The
140 terms R and SD are the temporal correlation coefficient, and the standard deviation of the corresponding time series, respectively. TCI is calculated using day-to-day time series grouped by local hour h, so that 24 separate coupling indices are calculated at each flux site for each month. This approach avoids the aforementioned problem of spurious diurnal soil moisture biases due to the dielectric sensor errors; the daytime bias is ameliorated by only combining data from the same time of day, and correlations are insensitive to the absolute magnitudes of data, thus minimizing the contribution of diurnal sensor errors.
145 Depending on the source and target variables, we can define different land and atmospheric coupling indices. For the land leg, SWC1 is commonly the source variable, and either H or LE is the target variable. These two land couplings are referred to as $L(SWC1, H)$ and $L(SWC1, LE)$. For the atmospheric leg, LCL is chosen as the target variable and H and LE are the source variables; the two atmospheric couplings are $A(H, LCL)$ and $A(LE, LCL)$. Additionally, Dirmeyer et al. (2014) extended the terrestrial coupling index and proposed the integrative L–A feedback metrics by combining the land and atmospheric legs.
150 This quantifies the two-legged coupling process initiated from soil moisture variability, carried through to the response of the atmosphere. It is formulated as:

$$TCI_h(SV_h, IV_h, TV_h) = R(SV_h, IV_h) \times R(IV_h, TV_h) \times SD(TV_h) \qquad (3)$$

where IV is the intermediate variable, here the surface fluxes. The two-legged coupling process is mediated by LE or H and source and target variables are always SWC1 and LCL, respectively. They are referred to as the total couplings $T(SWC1, H, LCL)$ and $T(SWC1, LE, LCL)$, the first indicating a pathway via the energy cycle, and the second through the
155 water cycle.

As the sensitivity of the land, atmospheric, and two-legged couplings is not symmetric depending on the pathway through different land surface fluxes, this study investigates their asymmetric behaviour in different coupling segments on the sub-daily time scale.

160 3.3 Mixing diagrams

A mixing diagram is a diagnostic relationship among components of the local L–A coupling process used to understand the integrative moist and thermal energy budget evolution in the mixed layer. It was first introduced by Stommel (1947) who addressed the coevolution of 2-m potential temperature (θ) and humidity (q) to the energy and water budgets during daytime PBL growth as a trajectory in a two-dimensional phase space of heat and water. Mixing diagrams break down the evolution of

165 θ and q into land and atmospheric components in which the flux contributions of surface heat (sensible) and moisture (latent) result in a land vector in the phase space whose slope corresponds to the Bowen ratio. The remaining components of their trajectories result from various atmospheric process (relevant to PBL entrainment, advection, condensation, evaporation and radiative transfer) (Betts, AK, 1992). Modelling studies have shown the sensitivity of the coevolution of θ and q to land and boundary layer physics schemes can be evaluated directly against observations (Santanello et al., 2009, 2011).

170 As near-surface or mixed-layer temperature and humidity, surface fluxes, and PBL height information are required to construct a mixing diagram, this integrative metric can also be applied with other data sources such as in-situ flux observations and ground-based active remote sensing products. Therefore, this study employs flux site observations to depict the observed coevolution of θ and q within the PBL on sub-diurnal time scales. Flux sites provide 2-m temperature (which is converted to θ) and q, atmospheric pressure, and when q is not available, vapor pressure deficit (VPD which is used along with pressure and temperature to calculate vapor pressure, and then q). θ and q are converted to energy variables, via multiplication by the

175 specific heat capacity of air (C_p=1005 J/kg·K) and the latent heat of vaporization (L_v =2.5x10^6 J/kg) respectively. The mixing diagram is constructed with hourly vectors ($V(t)$, t is the local hour), which consist of changes in thermal (specific dry enthalpy) and moisture (water vapor latent heat content) terms on the y- and x-axes respectively: $[\theta(t+1) - \theta(t)]C_p$ and $[q(t+1) - q(t)]L_v$. These terms are broken down into the hourly land and atmospheric vector components in this thermal-

180 moisture phase space.

For the estimation of the land surface contributions to PBL heat and humidity in the mixing diagram methodology, the vertically averaged temperature and pressure are needed within the PBL to estimate the mean PBL air density ($\bar{\rho}$). These are not available from near-surface measurements at flux towers. The temperature at the PBL top (T_{PBL}) is approximated by applying a temperature lapse rate of 6.5 K/km at the Z_{PBL} and the ML temperature ($\bar{T}$) is defined by the average of the 2-m

185 temperature and the PBL temperature. The vertical pressure gradient ($dP/dZ = -\rho g$ where P, Z, and g are air pressure, vertical depth, and gravitational acceleration of 9.8 m/s^2, respectively) and the ideal gas law ($P = \rho RT$ where is gas constant

of 287.058 J/kg·K) are used to obtain the pressure at the PBL top. When the density term in the vertical pressure gradient equation is replaced by the ideal gas law, we obtain:

$$\frac{dP}{dZ} = -\frac{Pg}{RT} \tag{4}$$

Taking the integral of both sides, the pressure at the PBL can be estimated as:

$$P_{PBL} = e^{-\frac{g}{R}(\ln T_{PBL} - \ln T_{2m}) + \ln P_{sfc}} \tag{5}$$

190 The mean ML pressure ($\bar{P}$) is approximated by the average of atmospheric pressure (P_{sfc}) and P_{PBL}. Then, the hourly ML air density ($\bar{\rho} = \bar{P}/R\bar{T}$) is recovered using the ideal gas law. Based on these estimated variables, the hourly land vector component (units: J/kg/hr) consists of surface heat (H_{sfc}) and moisture (M_{sfc}) terms attributed to sensible and latent flux contributions to the PBL. They are formulated following Santanello (2009):

$$H_{sfc}(t) = \frac{\bar{H}(t)}{\bar{\rho}(t)\, Z_{PBL}(t)} \Delta t \tag{6}$$

$$M_{sfc}(t) = \frac{\overline{LE}(t)}{\bar{\rho}(t)\, Z_{PBL}(t)} \Delta t \tag{7}$$

Each is calculated from hourly averaged sensible ($\bar{H}$) and latent ($\overline{LE}$) heat fluxes where Δt is one hour, i.e., 3600 seconds.

195 Next, the hourly atmospheric vector components are calculated as residuals of the hourly total vectors minus the land vectors, also consisting of surface heat (H_{atm}) and moisture (M_{atm}) terms. Both the thermal term and moisture term are implicitly defined by entrainment at the top of the boundary layer, horizontal advection, and phase changes of water in the ML. The thermal term for the atmosphere also includes the effects of radiative heating, cooling, and frictional warming. Their formulations are followed as:

$$H_{atm}(t) = C_p[\theta(t+1) - \theta(t)] - H_{sfc}(t) \tag{8}$$

$$M_{atm}(t) = L_v[q(t+1) - q(t)] - M_{sfc}(t) \tag{9}$$

200 Furthermore, the timely accumulated heat ($\sum H$) and moisture ($\sum M$) terms for the land and atmospheric component, respectively, are defined to characterize the accumulated diurnal budgets in the ML. They are formulated as:

$$\sum H_{comp}(t) = \sum_{h=0}^{t} H_{comp}(h) \tag{10}$$

$$\sum M_{comp}(t) = \sum_{h=0}^{t} M_{comp}(h) \tag{11}$$

where $comp$ is either sfc or atm and h is the hour, accumulations begin at 0000 LST.

One thing that should be remembered is that the '2-m assumption' for θ and q is embedded in this approach. The original concept in the mixing diagram is that θ and q represent mean values within the ML. Using 2-m values to represent mean ML

205   values assumes a perfectly mixed ML, and introduces error into calculations. For instance, 2-m temperature is higher (lower)
during daytime (night-time) than that in the ML along with the similar issues for humidity. The large near-surface radiative
cooling at night is significant even though this is quite decoupled from the ML. Thus, the '2-m assumption' leads to amplified
(reduced) budgets in the mixing diagram during daytime (night-time) due to atmospheric vectors, whereas the land vectors are
not affected as they are defined by the surface fluxes. The adaptation of the flux site data is an alternative approach to

210   understand the observed climatology of the coevolution of moist and thermal energy budgets in the ML because there are
difficulties to estimate the Z_{PBL} and to observe the vertical θ and q profiles. This assumption does not prevent exploration of
the general characteristics of the diurnal cycle and the precise comparison of a model to observations is possible if one also
uses the 2-m variables from the model.

215   **3.4 Methodology to separate water– and energy–limited regimes**

This study attempts to understand the local sensitivity of the L–A coupling processes in different climate regimes using the
analysis approach described above, as the effects of mesoscale meteorology are difficult to isolate. Water- and energy-limited
regimes, which indicate whether land heat fluxes are sensitive to the variability of the soil moisture, are categorized at the
observed sites to investigate the climate sensitivity of L–A interactions. The proxy to separate the regimes is the temporal

220   correlation between daily mean time series of SWC1 and evaporative fraction $EF = LE/(H + LE)$, which bridges heat and
moisture fluxes. Large positive correlations indicate a strong dependence of EF on variations in SWC1, signifying a water-
limited regime; negative correlations suggest an energy-limited regime. This study compares the sensitivity of the L–A
interactions to those different regimes between the top and bottom 10% of the observation sites sorted by the value of this
correlation. When the correlation is higher than 0.36 and the corresponding p-value is less than 0.005 (also requiring a sufficient

225   sample size at the flux site), the sorted observations are representative of the water-limited regime. When the correlation is
lower than 0.08 and the corresponding p-value is lower than 0.16, the sorted observations are defined as representative of the
energy-limited regime.

4 Results

230   **4.1 Asymmetric coupling behaviour in sub-daily time scale**

Before investigating the diurnal L–A coupling processes, we provide a comparison of the coupling metrics for the daily mean,
midday, and midnight periods for the different land surface fluxes (i.e., LE and H). Soil moisture has a proportional relationship
to LE based on the water balance, which results in positive values of the coupling metric $L(SWC1, LE)$ when energy is not
limited. As increasing LE leads to a decrease of H via the energy balance, $L(SWC1, H)$ is typically negative. Most of the flux

235   sites show these physical tendencies (Fig. 2a), which are related to the fact that many of the sites are located in summertime

water-limited regimes that correspond to "hot spots" of L–A coupling (Dirmeyer, 2011). The land coupling term shows a statistically significant negative relationship between $L(SWC1,H)$ and $L(SWC1,LE)$ for the daily mean, midday, and midnight periods. However, the characteristics of $L(SWC1,H)$ and $L(SWC1,LE)$ are not simply symmetric to each other. For instance, although they have in common that midday coupling variability is greater than that of the daily mean or midnight

240   due to large net radiation, $L(SWC1,LE)$ for all periods shows little mean difference and nested distributions across sites, whereas mean $L(SWC1,H)$ shows larger differences and clear shifts in distributions (Fig 2a). This means that the asymmetry of $L(SWC1,H)$ in the sub-daily time scale is larger than that of $L(SWC1,LE)$, a characteristic that is explored in more detail later.

Fig. 2b shows the atmospheric couplings. The relationship between $A(H,LCL)$ and $A(LE,LCL)$ is not significant during

245   midday due to their opposite relationships on either side of $A(LE,LCL) = 0$. This is clearly shown in their density function, in which $A(LE,LCL)$ has peaks on both positive and negative sides of zero even though $A(H,LCL)$ has only one peak on the positive side. The result in the positive $A(LE,LCL)$ and $A(H,LCL)$ situation occurs in energy-limited locations whereby increased net radiation leads to increasing LE and H along with rising temperature, which subsequently induces the LCL increase. In contrast, the result in the negative $A(LE,LCL)$ case is explained by the water-limited processes such that decreasing

250   LE leads to decreasing relative humidity and dew point temperature, which subsequently induces the LCL increase. Although these physical atmospheric coupling processes are not seen during the night-time, the daytime processes dominate the daily mean result. Moreover, if $A(H,LCL)$ is greater than $A(LE,LCL)$, it means that the boundary layer is more sensitive to H, and vice versa. The higher $A(H,LCL)$ during the daytime is due to the stronger correlation between H and LCL, and the higher $A(LE,LCL)$ during the night-time is attributed to the negative H.

255   The observed two-legged couplings from soil moisture to LCL, mediated by H and LE, are mostly negative (Fig. 2c), which means LCL height is anticorrelated with soil moisture regardless of the pathway of coupling. Points on the right of the diagonal x=y line indicate stronger two-legged coupling through LE than through H, which arise mainly from the larger correlation terms of land and atmosphere coupling via LE. Also, the LCL is less sensitive to H variability compared with LE in dry land conditions (not shown). Although there is a clear difference in both two-legged couplings between midday and midnight, the

260   density distributions of the LE-mediated coupling for the daily mean and the midday are similar. In contrast, that related to H is quite different: the midday result exhibits more negative mean coupling and is more widely distributed. Both are commonly negatively skewed in the entire sub-daily time span, and it is attributable to the atmospheric coupling.

The land coupling tends to be stronger when the climate is relatively warm and dry, and the effect is more pronounced during midday than midnight (Figs. 3a and 3d). Although there is a clear difference between $A(LE,LCL)$ and $A(H,LCL)$ for midday

265   and midnight, the climate sensitivity of both atmospheric couplings according to the range of soil moisture is very different for moisture versus energy coupling pathways (Fig. 3b). For instance, the response of the $A(LE,LCL)$ to changing soil moisture shows negative values as the soil dries out due to water limitations and positive values that increase as the soil gets wetter due to energy limitations (c.f., Fig. 2b). However, $A(H,LCL)$ is much less sensitive.

In contrast, the sensitivity of $A(H, LCL)$ to temperature is comparable to $A(LE, LCL)$ and the moisture pathway results from
270 the soil moisture categorization (warm temperatures usually correspond to dry soil). The midday $A(H, LCL)$ coupling strength
decreases as temperatures warm, but the coupling is dramatically increased in the warmest category, in which the $A(LE, LCL)$
becomes negative (Fig. 3e). The H-driven coupling sensitivity is attributed to the temperature sensitivity of the correlation
$R(H, LCL)$. The incoming radiation in hot climates is mostly transferred to the H, limiting humidity increase, which results in
strong sensitivity between H and LCL. The daily mean reflects the midday result as there is little contribution from overnight
275 processes.

Meanwhile, the sensitivity of two-legged couplings to soil moisture and temperature also differs, and their characteristics are
most pronounced in the daytime. The sensitivity of $T(SWC1, LE, LCL)$ to soil moisture during midday (Fig. 3c) is high in
relatively dry climates despite less change in $T(SWC1, H, LCL)$, which is mostly attributed to the effects of the atmospheric
leg. Conversely, in relatively wet climates, $T(SWC1, H, LCL)$ is highly sensitive to soil moisture despite muted changes in
280 $T(SWC1, LE, LCL)$, as $L(SWC1, H)$ represents a larger contribution to the sensitivity to soil moisture than does $L(SWC1, LE)$.
The midday results have a similar sensitivity to the daily mean despite the lack of sensitivity at night. The results categorized
by temperature show strong coupling in $T(SWC1, H, LCL)$ and $T(SWC1, LE, LCL)$ only for the warmest days during both
midday and midnight because of the temperature sensitivity in the atmospheric coupling (Fig. 3f). There are also categorical
coupling sensitivities across different land covers (Fig. S1). For instance, wetlands generally agree with the results for wet and
285 cold climates and coupling for savanna sites is consistent with the results shown in Fig. 3 for dry and warm climates.

4.2 Diurnal mixing diagrams

In this subsection, we explore the full 24-hour diurnal mixing diagrams for a comprehensive understanding of the water and
energy budget evolution in the boundary layer relevant to the L–A interactions. First, the diurnal L–A couplings are averaged
290 across 230 observation sites to illustrate climatological behaviour (Fig.4). Panels a-c are constructed in the same manner as
mixing diagrams, with moisture variability along the x-axis and heat variability on the y-axis, but instead plot the daily
evolution of the two-legged, terrestrial and atmospheric couplings, respectively. During the daytime, both two-legged
couplings are negative, with $T(SWC1, H, LCL)$ being almost three times as strong as $T(SWC1, LE, LCL)$ around midday,
showing the importance of sensible heating for ML growth (Fig. 4a). The sign of the two-legged coupling is determined by
295 the multiplication of the correlation terms, representing land and atmospheric couplings. $R(SWC1, H)$ and $R(H, LCL)$ are
mostly distributed on negative and positive sides, respectively, leading to consistently large magnitudes. On the contrary,
$R(SWC1, LE)$ and $R(LE, LCL)$ span 3 of the 4 quadrants, so do not result a consistent sign, reducing the mean magnitude (Fig.
S2). Both of the two-legged metrics contain the same standard deviation term, so it is the correlations that lead to larger
negative mean values of $R(SWC1, H) \times R(H, LCL)$ than the corresponding pathway via LE. There is also hysteresis such that

300   the thermal process chain leads the moist process chain by 2-3 hours during the day. The thermal coupling collapses toward zero quickly in the late afternoon, while the moist coupling declines gradually throughout the evening.

In the land leg, $L(SWC1, H)$ and $L(SWC1, LE)$ attain large negative and positive values respectively during the daytime, with the stronger $L(SWC1, H)$ about double the magnitude of $L(SWC1, LE)$ (Fig. 4b). The diurnal growth and decay of the coupling strengths also exhibit some hysteresis with the phase of $L(SWC1, H)$ leading $L(SWC1, LE)$ by about an hour, in contrast to

305   the surface fluxes themselves whereby the thermal fluxes lead the moisture fluxes. Couplings peak about noon and are near zero throughout the night-time hours.

For the atmospheric couplings (Fig. 4c), there is a more complex evolution. $A(H, LCL)$ is positive during the day and negative at night, while $A(LE, LCL)$ is positive across the entire day. Each reaches a maximum during the early afternoon, and the coupling strength of $A(H, LCL)$ is double that of $A(LE, LCL)$, due to higher $R(H, LCL)$. The diurnal coevolution again reveals

310   hysteresis with abrupt decaying of $A(H, LCL)$ from 3-7 PM. $A(LE, LCL)$ peaks in strength about 4 PM dropping quickly to a minimum at 8 PM before beginning a gradual 20-hour rise. The result is a figure-eight path in Fig.4c.

The observationally-based diurnal mixing diagram (Fig. 4d) shows the climatological coevolution of moisture and thermal energy budgets within the ML. The path of the ML specific dry enthalpy and water vapor latent heat content trace a banana-shaped pattern, with a strong diurnal cycle of heat content, but a clear semi-diurnal cycle for moisture. Note that the daily

315   means are not enveloped within the hourly path on the mixing diagram. The daily mean ML potential temperature and humidity are not experienced at the same time at any hour of the day, and the ML budget exchange processes in the sub-daily time scale experience strong hysteresis. There is commonly an increase in both moist and thermal energy per unit mass from 4 AM to 8 AM, after which moist energy decreases until 3 PM while thermal energy keeps increasing. This is followed by a decrease in thermal energy while the moisture energy increases until 7 PM and then decreases until the next morning.

320   To identify the distinct roles of land and atmosphere in the diurnal mixing diagram evolution, we examine the hourly component vectors from surface fluxes (Fig. 4e) and atmospheric processes (Fig. 4f). On average across every hour of the day, moisture is supplied by surface evaporation (Fig. 4e). Daytime evaporation and transpiration is strong, but night-time transpiration and surface evaporation appear to exist in the hourly mean data. Meanwhile, there is thermal energy loss during the night-time and gain during the daytime. The net moist and thermal energy gain or loss during the entire day attributed to

325   land surface processes can be defined by the vector from the origin to point 23. The length of each hourly vector indicates the rate of change of heat content contributed by surface fluxes, portrayed in Fig. 4g in terms of energy per unit mass of air per hour. The rates are highest in the morning and gradually decreases in the afternoon because Z_{PBL} reaches maximum around 2 PM, maximizing the volume of the reservoir accepting the surface fluxes. Because of the strong relationship between the mean and the variance of land heat fluxes, the corresponding land couplings also have a strong correlation with the mean value.

330   However, the land vectors are somewhat different from the land couplings since the vectors are also affected by the diurnal variability of the Z_{PBL} (Eq 4 and 5). The time series of diurnal land tendencies in Fig. 4g outline an ellipse, M_{sfc} remaining

positive at all hours. Moisture and thermal tendencies abruptly increase at sunrise, reaching a maximum in early to mid-morning with M_{sfc} peaking about two hours before H_{sfc}, then both tendencies gradually decrease until midnight.

On the other hand, the accumulated atmospheric components (Fig. 4f) show a gradual daylong decrease in moist energy, while

335   there is gradual thermal energy increase from the sunrise to around the noon, then a decrease until midnight. The only moistening through the day is very small, occurring between 5-7 AM and around 5 PM (Fig. 4h). The positive temperature and negative moisture tendency from 7 AM to the noon is mostly related to the entrainment drier air with higher potential temperature at the top of the growing boundary layer. The negative tendency of thermal energy from the afternoon onward is likely dominated by radiative cooling (Betts et al., 1996), although advection and phase changes due to condensation,

340   precipitation and reevaporation may also contribute. Drying afternoon is likely due to net moisture diffusion into the free atmosphere from the ML, and removal of water vapor from the air by condensation in clouds. These effects combine to produce an "omega" path in the diurnal atmospheric components (Fig. 4f). Although the daily mean is not enveloped within the hourly evolution on the mixing diagram (Fig. 4d), the daily mean values of both land and atmospheric vector components are enveloped by their diurnal paths (Fig. 4g and h), emphasizing that the ML budget exchange processes at sub-daily time scales

345   is a complex interaction of surface and atmospheric processes.

4.3 Climate regime dependence

Additionally, we examine the sensitivity of the diurnal budget coevolution and the L–A interactions separately for water– and energy–limited regimes. Based on the aforementioned approach to separate those regimes (Sec. 3.4), we have composited the

350   upper and lower 10% observation sites. The average soil moisture and temperature of the water–limited observation sites are 0.13 m³/m³ and 23.6 °C, respectively; for energy–limited sites they are 0.29 m³/m³ and 19 °C, respectively.

The three segments of diurnal L–A couplings over the water–limited regions show different sub-daily pathways and stronger couplings than for the energy–limited sites (Fig. 5). Although the coupling strengths for both sets are maximized during the daytime, the diurnal coevolution of two-legged couplings (Fig. 5a) in the water–limited sites resembles more closely the

355   climatological series (cf., Fig. 4a), but stronger, while the energy–limited sites have very weak couplings. For the land couplings, the diurnal behaviour for the water–limited sites shows characteristically negative $L(SWC1, H)$ and positive $L(SWC1, LE)$ with comparable coupling strengths between them (Fig. 5b). Over energy–limited sites, $SWC1$ and LE are anticorrelated as evaporation controls soil moisture. Dry soils still correspond to deeper boundary layers, but the magnitudes of the coupling metrics are a fraction of their moisture-limited counterparts. Neither of these extreme composites shows much

360   diurnal hysteresis.

In the climate sensitivity of atmospheric couplings (Fig. 5c), there is a strong divergence of behaviours. Although $A(H, LCL)$ over the water–limited regime is stronger than over the energy–limited regime, both show a diurnal evolution of $A(H, LCL)$ that is negative at night, grows strongly positive through the morning peaking a couple hours after local noon. However, $A(LE, LCL)$ is highly divergent between the water– and energy–limited regimes. While comparable in magnitude, water

365   limited regimes show anticorrelation between surface evaporation and LCL height throughout the day, peaking twice (around
noon, then more strongly at sunset), while the energy-limited regime registers positive correlations all day and a single mid-
afternoon peak. The water–limited result for $A(LE, LCL)$ is attributed to the proportional relationship of LE as a source of
water vapor to relative humidity and dew point temperature leads to an anticorrelation LCL height (c.f., Fig. 2b). The results
for energy-limited sites are not attributable to direct surface forcing of LCL or ML characteristics, but rather the dominance of

370   atmospheric dynamics and circulation in determining both near-surface meteorology and surface flux rates. Warm periods
correspond to more net radiation and stronger evaporation at the same time the LCL is higher, while cool moist periods limit
both LCL height and latent heat flux.

The observed diurnal mixing diagrams also exhibit the diurnal banana-shaped paths, but the water– and energy–limited regions
reveal different long tails (Fig. 5d). Both show a morning peak in ML humidity, but the driest time for the ML is during early

375   afternoon in moisture-limited regimes, but before sunrise in moisture-limited regimes. Both regimes span mostly the same
range of water vapor latent heat content, but they have little overlap in terms of dry enthalpy. Also, the daily means are not
enveloped within the hourly path for either regime, but they lie closer to their respective paths compared to Fig. 4d. Dry
regimes also exhibit much greater hysteresis. The differences are mostly induced by differing moist budget evolution in land
and atmospheric components. For instance, the daytime long tail is related to the small moisture increase due to the relatively

380   smaller mean LE along with soil dryness, so that the atmospheric entrainment makes large drying in the ML. The early morning
long tail results from the large moist budget decrease by the atmospheric effects during the afternoon and there is a large
moisture increase by the land surface along with a reduced moisture decrease by the atmosphere from 4 AM to 8 AM.

To identify the distinct climate sensitivity of land and atmosphere in the mixing diagram, we examine the hourly component
vectors (Fig. 5e and f). Despite the comparable incoming net radiation at the land surface, the partitioning of the net radiation

385   to the LE and the H (e.g., the Bowen ratio) differs between the separated climate regimes, which results in an overall net gain
and loss in the heat or moisture budgets across the entire day. In the water–limited regime, the arid surface conditions lead to
less LE, with the extra energy going toward H, which drives the large increases in heat energy during the daytime even though
there is a larger loss of thermal energy during the night-time (larger negative H; Figs. 5e and 5g). For energy-limited regimes,
moisture fluxes are larger and thermal fluxes are smaller.

390   The atmospheric components for the diurnal mixing diagram (Fig 5f and h) also show a distinct climate sensitivity in the ML
moisture dimension even though the climate regimes are separated by the characteristics of land coupling processes described
above. In the energy–limited regime, the positive moist tendency due to evaporation around sunrise starts about half an hour
earlier than for the moisture-limited regime since the sun rises earlier on average at the energy-limited flux sites as they tend
to be at higher latitudes (Fig. 5h). Moreover, there is a larger negative moisture tendency from afternoon to next early morning,

395   which characterizes the larger atmospheric moisture loss over the energy–limited regime (Fig. 5f). Interestingly, the moisture
limit regimes show two periods of atmospheric-driven ML moistening during the day: from 5-7 AM but also from 4-9 PM.
We could only speculate on the causes in the composites, but investigation of individual flux tower sites in semi-arid regions
near moisture sources (e.g., irrigated farmland) do show evidence of moist advection during the afternoon (not shown).

5 Conclusions

400

Most previous studies exploring L–A interactions have been restricted to daily or lower frequency time domains because of the limited availability of data resolving the diurnal cycle and inherent sensor issues that make it difficult to measure sub-daily variability. Although coupling characteristics between the daytime and night-time are obviously different due to the large disparity in available energy, namely incoming solar radiation, this research area has been underexplored. Nowadays, there 405 are an increasing number of long-term flux tower data available measuring land surface and near-surface atmospheric variables at hourly or finer time resolution across the globe. The baseline for such observational datasets is FLUXNET2015, and the AmeriFlux and the European Fluxes Database are additionally used to extend data availability spatially or temporally for this study. Here, we have described the climatology of the observed L–A interactions at sub-daily time scales during the local summer season across 230 sites (Fig. 1).

410 To measure the response of the target variables to the representative variability of the source variables in the L-A coupling paradigm (Santanello et al., 2018) in a chain from land states to surface fluxes and atmospheric characteristics, this study adopts multivariate metrics that define land, atmospheric, and combined couplings through both the water and energy cycles. To understand the heat and moisture budget exchanges within the ML, the mixing diagram approach has been adapted to extend the relationship between the coevolution of the budgets and L-A couplings across the entire day. We have quantified 415 the mean condition across sites and distributions, with a particular focus on the most water-limited and energy-limited sites with regard to surface fluxes. We find the diurnal cycles of both mixing diagrams and hourly L-A couplings usually exhibit hysteresis – the evening path through the water-energy phase space does not retrace the morning path. Using hourly observations, information from the coupling metrics and mixing diagrams has been synthesized to reveal in great depth the evolution of L-A interactions across the diurnal cycle, and to differentiate unique behaviours in energy-limited and water-420 limited regimes.

Segmented coupling metrics for the land leg (L), the atmospheric leg (A), and joint two-legged (T) metrics are compared among entire daily mean, daytime, and night-time periods for moisture (LE) and thermal (H) pathways. The land leg couplings (Fig. 2a) show significant negative relationships between $L(SWC1, LE)$ and $L(SWC1, H)$ across sites for the daily, midday, and midnight averages. This result is explained by the proportional relationship between soil moisture and LE based on the 425 water balance equation and the negative relationship between soil moisture and H. The diurnal land coupling evolution exhibits a hysteresis with the phase of $L(SWC1, H)$ leading $L(SWC1, LE)$ by about an hour. $L(SWC1, H)$ mostly attains negative value regardless of the hour of day and background climates whereas $L(SWC1, LE)$ is negative and positive in the energy-limited and water-limited regimes, respectively. The land couplings tend to be stronger as the climate becomes warmer or drier (water-limited regime), also evident in Figs. 3a, 3d and 5b, and the effect is more pronounced during the daytime.

430 Regarding atmospheric couplings, the diurnal phase shift in $A(H, LCL)$, which shows daytime positive and night-time negative correlations, is consistent regardless of the climate regimes (Fig. 5c). The coherent night-time negative correlation is attributed

to the physical process chain such that large negative H, indicating a large temperature gradient between colder ground and warmer boundary layer, induces the LCL increase (Fig. S3b). $A(H, LCL)$ is rather insensitive to soil moisture variations, and daytime $A(H, LCL)$ tends to weaken as mean temperature increases up to the warmest category ($T>26°C$) where coupling
435   strength abruptly increases (Fig. 3e). In contrast, $A(LE, LCL)$ reveals a clear sensitivity to climate regime because as LE decreases, LCL necessarily increases in water-limited locations, but where energy is limited, meteorological variations drive both LCL height and evaporation rates (Fig. 5c). The diurnal atmospheric coupling evolution represents positive and negative peaks at early afternoon and midnight, respectively, and exhibits hysteresis with the phase of $A(H, LCL)$ leading $A(LE, LCL)$ by about two hours. Moreover, the atmospheric couplings (especially the correlation component) commonly weaken
440   nonlinearly whereas the functional relationship of the H is stronger than that of the LE (Fig. S3).

The corresponding integrated two-legged couplings, $T(SWC1, LE, LCL)$ and $T(SWC1, H, LCL)$, are mostly negative (Fig. 2c), meaning dry soils correspond to a higher cloud base. The stronger daytime values of $T(SWC1, H, LCL)$ suggest variations in H exert more control on LCL than variations in LE. The daytime values of $T(SWC1, LE, LCL)$ and $T(SWC1, H, LCL)$ are highly sensitive to soil moisture variations toward the dry and wet ends of the soil moisture distribution, respectively (Fig. 3c),
445   marking very different behaviours between dry and wet regimes, but there is little sensitivity to the temperature except, again, at the warm extreme (Fig. 3f). The stronger two-legged couplings in a warm and dry climate (water-limited regime) result from the combination of larger negative correlation ($R(SV, IV) \times R(IV, TV)$) and higher variability of the LCL.

In many previous studies, only a daytime budget analysis using mixing diagrams has been conducted, but this study covers the entire diurnal cycle. The results of the full diurnal mixing diagrams (Figs. 4 and 5) show that the path of ML specific dry
450   enthalpy and water vapor latent heat content across all 24 hours traces a banana shaped path, and the different phases of heat (a single peak in early afternoon) and moisture (a double peak) mean the daily average state of the ML is not actually experienced at any hour of the day (Fig. 4d). The diurnal mixing diagram breaks down the hourly vector of θ and q into land and atmospheric components. The land vector components show added moisture from evaporation across the entire day, but a thermal energy gain (loss) during the daytime (night-time) depending on the sign of H (Fig. 4e). Thus, the net contribution of
455   LE to the total daily energy budget in the ML is larger than from H. The individual diurnal evolutions of surface fluxes and PBL depth result in a maximum of positive humidity and temperature tendencies during the morning (Fig. 4g). The peak hourly coupling strength occurs after the maximum heat and moisture tendencies occur. The diurnal atmospheric components are calculated as residuals the mixing diagram minus land surface flux contributions, and represent a synthesis of many effects (e.g., PBL entrainment, horizontal advection, radiative cooling, and etc), which produces an "omega" path in hourly
460   atmospheric vectors of ML humidity and temperature (Fig. 4f). The entrained dry and warm air at the top of the PBL causes the positive temperature and negative moisture tendencies from 7 AM to noon. When the net ML dry enthalpy supplied by entrainment is near its diurnal maximum, the atmospheric couplings tend to be strongest.

The water– and energy–limited processes represent a large discrepancy in the ML specific dry enthalpy despite a small difference of water vapor latent heat content (Fig. 5d). The 24-hour mixing diagram for water-limited processes exhibits much
465   greater hysteresis, which means the large asymmetricity in the water-energy phase space across the entire day. The climate

regimes also exhibit opposing long tails of minimum water vapor content: whether a location experiences the driest ML just before sunrise or in the afternoon depends on the balance of competing drivers: land surface evaporation adding moisture and entrainment mixing dry air into the ML. In water-limited regimes, entrainment dominates and minimum $L_v q$ occurs when dry enthalpy peaks. In energy-limited regimes, minimum $L_v q$ occurs when the air is coolest, consistent with the Clausius–

470 Clapeyron theory in which the temperature decrease reduces the water-holding capacity of the air. Regarding the climate sensitivity in the land component vectors, the partitioning of the net radiation into LE and H shows correspondence to the climate regimes (Fig. 5e). In a water–limited regime, larger H and smaller LE during the daytime lead to a larger maximum, net, and range of thermal energy than in the energy–limited regime, but greater moistening across the day in the energy-limited regime. The difference in net moisture and thermal energy gain depends on the climate regime: the larger being around 60%

475 greater than the smaller in each regime. Interestingly, despite having smaller net surface radiation during the day, energy-limited regimes appear to have a greater 24-hour net surface energy contribution from the land surface $\sum(M_{sfc} + H_{sfc})$ than moisture-limited regimes due to their higher total evaporation and less overnight sensible heat loss from atmosphere to land; the difference in energy per unit mass is around 35-40% (comparing markers labelled "23" in Fig. 5e).

Overall, this study suggests there is more to be learned about L–A interactions by comprehensive study of sub-daily time scales.

480 The asymmetric diurnal evolution of the land, atmosphere and combined coupling metrics as well as within the 24-hour path of ML water and energy content portrayed in the mixing diagrams begs further study. With additional data, particularly profile measurements within and above the atmospheric boundary layer, it would be possible to begin to decompose the atmospheric evolution into its component terms, separating advection from entrainment and other diabatic processes. We can imagine a role for single-column models as useful diagnostic tools to aid further study. The metrics introduced in this study could also

485 be applied to understand and evaluate the diurnal cycle of L–A interactions in models. Essentially, this study makes the case for the need to attend to sub-daily processes for a better understanding of L–A coupling, even while much research is still focused on evaluations based on daily data. Data availability remains a limitation; we hope work such as this can motivate the collection of more data that resolves the diurnal cycle over land.

Lastly, it should be noted that the diagnoses presented here presume the fidelity of the flux tower measurements, but there are

490 known biases and a distinct lack of energy balance closure at most sites (Cheng et al., 2017). The assumptions of Monin-Obukhov similarity theory, widely applied for flux tower calculations and in many model parameterizations, are compromised in many situations (Wulfmeyer et al., 2018) including variations across the diurnal cycle and inconsistencies between moisture and thermal fluxes (Van De Boer et al., 2014). These problems may affect details of the diurnal cycles in the figures presented here, particularly when trends or rates of change are marginal. However, we feel the main features shown here are likely robust,

495 and certainly worth closer investigation. Mean biases do not affect correlations or standard deviations, which are at the heart of the coupling metrics, but diurnally dependent biases could affect some results presented here. Within the limits already inherent in coupling metrics, the results presented here are consistent with current process understanding yet shed new light on the relationships between energy and water cycles, between land and atmosphere, by combining and extending existing approaches in a novel way.

Acknowledgements

This study was supported by NOAA grant NA19NES4320002 to the Cooperative Institute for Satellite Earth System Studies (CISESS) at the University of Maryland/ESSIC via a subaward (79785-Z755420) to the Center for Ocean-Land-Atmosphere Studies at George Mason University. We also wish to thank Hsin Hsu for constructive comments which helped us improve the manuscript.

Code availability

The source code used in this study is shared on the GitHub (https://github.com/ekseo/Diurnal_LA_coupling.git).

Data availability

Flux tower observations that support the findings of this study are openly available in from the FLUXNET2015 Tier 1 data (https://fluxnet.fluxdata.org/), the AmeriFlux network (https://ameriflux.lbl.gov/), and the drought-2018 network (https://doi.org/10.18160/YVR0-4898). The Copernicus Climate Change Service (C3S) provides access to ERA5 data freely through its online portal at https://cds.climate.copernicus.eu/cdsapp#!/dataset/reanalysis-era5-single-levels.

Author contribution

ES led manuscript writing and contributed to the data analysis. PD contributed to the research idea and manuscript writing.

Competing interests

The authors have no competing interests to declare.

References

Alemohammad, S. H., Fang, B., Konings, A. G., Aires, F., Green, J. K., Kolassa, J., Miralles, D., Prigent, C., and Gentine, P.: Water, Energy, and Carbon with Artificial Neural Networks (WECANN): a statistically based estimate of global surface turbulent fluxes and gross primary productivity using solar-induced fluorescence, Biogeosciences, 14, 4101-4124, 2017.

Benson, D. O. and Dirmeyer, P. A.: Characterizing the relationship between temperature and soil moisture extremes and their role in the exacerbation of heat waves over the contiguous United States, Journal of Climate, 34, 2175-2187, 2021.

Betts, A.: FIFE atmospheric boundary layer budget methods, Journal of Geophysical Research: Atmospheres, 97, 18523-18531, 1992.

Betts, A. K., Ball, J. H., Beljaars, A. C., Miller, M. J., and Viterbo, P. A.: The land surface-atmosphere interaction: A review based on observational and global modeling perspectives, Journal of Geophysical Research: Atmospheres, 101, 7209-7225, 1996.

Cheng, Y., Sayde, C., Li, Q., Basara, J., Selker, J., Tanner, E., and Gentine, P.: Failure of Taylor's hypothesis in the atmospheric surface layer and its correction for eddy-covariance measurements, Geophysical Research Letters, 44, 4287-4295, 2017.

Colliander, A., Jackson, T. J., Bindlish, R., Chan, S., Das, N., Kim, S., Cosh, M., Dunbar, R., Dang, L., and Pashaian, L.: Validation of SMAP surface soil moisture products with core validation sites, Remote Sensing of Environment, 191, 215-231, 2017.

Crow, W. T., Lei, F., Hain, C., Anderson, M. C., Scott, R. L., Billesbach, D., and Arkebauer, T.: Robust estimates of soil moisture and latent heat flux coupling strength obtained from triple collocation, Geophysical Research Letters, 42, 8415-8423, 2015.

Denissen, J., Orth, R., Wouters, H., Miralles, D. G., van Heerwaarden, C. C., de Arellano, J. V.-G., and Teuling, A. J.: Soil moisture signature in global weather balloon soundings, npj Climate and Atmospheric Science, 4, 1-8, 2021.

Dirmeyer, P. A.: The terrestrial segment of soil moisture–climate coupling, Geophysical Research Letters, 38, 2011.

Dirmeyer, P. A., Wang, Z., Mbuh, M. J., and Norton, H. E.: Intensified land surface control on boundary layer growth in a changing climate, Geophysical Research Letters, 41, 1290-1294, 2014.

Dirmeyer, P. A., Balsamo, G., Blyth, E. M., Morrison, R., and Cooper, H. M.: Land-atmosphere interactions exacerbated the drought and heatwave over northern Europe during summer 2018, AGU Advances, 2, e2020AV000283, 2021.

Dirmeyer, P. A., Gao, X., Zhao, M., Guo, Z., Oki, T., and Hanasaki, N.: GSWP-2: Multimodel Analysis and Implications for Our Perception of the Land Surface, Bulletin of the American Meteorological Society, 87, 1381-1398, 10.1175/bams-87-10-1381, 2006.

Dirmeyer, P. A., Chen, L., Wu, J., Shin, C.-S., Huang, B., Cash, B. A., Bosilovich, M. G., Mahanama, S., Koster, R. D., and Santanello, J. A.: Verification of land–atmosphere coupling in forecast models, reanalyses, and land surface models using flux site observations, Journal of hydrometeorology, 19, 375-392, 2018.

Dirmeyer, P. A., Wu, J., Norton, H. E., Dorigo, W. A., Quiring, S. M., Ford, T. W., Santanello Jr, J. A., Bosilovich, M. G., Ek, M. B., and Koster, R. D.: Confronting weather and climate models with observational data from soil moisture networks over the United States, Journal of Hydrometeorology, 17, 1049-1067, 2016.

Dorigo, W., Wagner, W., Albergel, C., Albrecht, F., Balsamo, G., Brocca, L., Chung, D., Ertl, M., Forkel, M., and Gruber, A.: ESA CCI Soil Moisture for improved Earth system understanding: State-of-the art and future directions, Remote Sensing of Environment, 203, 185-215, 2017.

Dorigo, W., Wagner, W., Hohensinn, R., Hahn, S., Paulik, C., Xaver, A., Gruber, A., Drusch, M., Mecklenburg, S., and Oevelen, P. v.: The International Soil Moisture Network: a data hosting facility for global in situ soil moisture measurements, Hydrology and Earth System Sciences, 15, 1675-1698, 2011.

Entekhabi, D., Njoku, E. G., O'Neill, P. E., Kellogg, K. H., Crow, W. T., Edelstein, W. N., Entin, J. K., Goodman, S. D., Jackson, T. J., and Johnson, J.: The soil moisture active passive (SMAP) mission, Proceedings of the IEEE, 98, 704-716, 2010.

Evans, J. G., Ward, H., Blake, J., Hewitt, E., Morrison, R., Fry, M., Ball, L., Doughty, L., Libre, J., and Hitt, O.: Soil water content in southern England derived from a cosmic-ray soil moisture observing system–COSMOS-UK, Hydrological Processes, 30, 4987-4999, 2016.

Findell, K. L. and Eltahir, E. A.: Atmospheric controls on soil moisture–boundary layer interactions. Part II: Feedbacks within the continental United States, Journal of Hydrometeorology, 4, 570-583, 2003a.

Findell, K. L. and Eltahir, E. A.: Atmospheric controls on soil moisture–boundary layer interactions. Part I: Framework development, Journal of Hydrometeorology, 4, 552-569, 2003b.

Findell, K. L., Gentine, P., Lintner, B. R., and Kerr, C.: Probability of afternoon precipitation in eastern United States and Mexico enhanced by high evaporation, Nature Geoscience, 4, 434-439, 2011.

Guo, Z., Dirmeyer, P. A., Koster, R. D., Sud, Y., Bonan, G., Oleson, K. W., Chan, E., Verseghy, D., Cox, P., and Gordon, C.: GLACE: the global land–atmosphere coupling experiment. Part II: analysis, Journal of Hydrometeorology, 7, 611-625, 2006.

Hersbach, H., Bell, B., Berrisford, P., Hirahara, S., Horányi, A., Muñoz-Sabater, J., Nicolas, J., Peubey, C., Radu, R., and Schepers, D.: The ERA5 global reanalysis, Quarterly Journal of the Royal Meteorological Society, 146, 1999-2049, 2020.

Kapilaratne, R. J. and Lu, M.: Automated general temperature correction method for dielectric soil moisture sensors, Journal of Hydrology, 551, 203-216, 2017.

Kerr, Y. H., Waldteufel, P., Wigneron, J.-P., Delwart, S., Cabot, F., Boutin, J., Escorihuela, M.-J., Font, J., Reul, N., and Gruhier, C.: The SMOS mission: New tool for monitoring key elements ofthe global water cycle, Proceedings of the IEEE, 98, 666-687, 2010.

Koster, R. D., Dirmeyer, P. A., Hahmann, A. N., Ijpelaar, R., Tyahla, L., Cox, P., and Suarez, M. J.: Comparing the Degree of Land–Atmosphere Interaction in Four Atmospheric General Circulation Models, Journal of Hydrometeorology, 3, 363-375, 10.1175/1525-7541(2002)003<0363:Ctdola>2.0.Co;2, 2002.

Koster, R. D., Dirmeyer, P. A., Guo, Z., Bonan, G., Chan, E., Cox, P., Gordon, C., Kanae, S., Kowalczyk, E., and Lawrence, D.: Regions of strong coupling between soil moisture and precipitation, Science, 305, 1138-1140, 2004.

Koster, R. D., Sud, Y., Guo, Z., Dirmeyer, P. A., Bonan, G., Oleson, K. W., Chan, E., Verseghy, D., Cox, P., and Davies, H.: GLACE: the global land–atmosphere coupling experiment. Part I: overview, Journal of Hydrometeorology, 7, 590-610, 2006.

Koster, R. D., Mahanama, S. P. P., Yamada, T. J., Balsamo, G., Berg, A. A., Boissiere, M., Dirmeyer, P. A., Doblas-Reyes, F. J., Drewitt, G., Gordon, C. T., Guo, Z., Jeong, J.-H., Lee, W.-S., Li, Z., Luo, L., Malyshev, S., Merryfield, W. J., Seneviratne, S. I., Stanelle, T., van den Hurk, B. J. J. M., Vitart, F., and Wood, E. F.: The Second Phase of the Global Land–Atmosphere Coupling Experiment: Soil Moisture Contributions to Subseasonal Forecast Skill, Journal of Hydrometeorology, 12, 805-822, 10.1175/2011jhm1365.1, 2011.

Lawrence, D. M., Hurtt, G. C., Arneth, A., Brovkin, V., Calvin, K. V., Jones, A. D., Jones, C. D., Lawrence, P. J., de Noblet-Ducoudré, N., and Pongratz, J.: The Land Use Model Intercomparison Project (LUMIP) contribution to CMIP6: rationale and experimental design, Geoscientific Model Development, 9, 2973-2998, 2016.

585 Ma, H., Zeng, J., Chen, N., Zhang, X., Cosh, M. H., and Wang, W.: Satellite surface soil moisture from SMAP, SMOS, AMSR2 and ESA CCI: A comprehensive assessment using global ground-based observations, Remote Sensing of Environment, 231, 111215, 2019.

Miralles, D., Van Den Berg, M., Teuling, A., and De Jeu, R.: Soil moisture-temperature coupling: A multiscale observational analysis, Geophysical Research Letters, 39, 2012.

Miralles, D. G., Gentine, P., Seneviratne, S. I., and Teuling, A. J.: Land–atmospheric feedbacks during droughts and heatwaves: state of the science and current challenges, Annals of the New York Academy of Sciences, 1436, 19-35, 2019.

590 Miralles, D. G., Jiménez, C., Jung, M., Michel, D., Ershadi, A., McCabe, M., Hirschi, M., Martens, B., Dolman, A. J., and Fisher, J. B.: The WACMOS-ET project–Part 2: Evaluation of global terrestrial evaporation data sets, Hydrology and Earth System Sciences, 20, 823-842, 2016.

Novick, K. A., Biederman, J., Desai, A., Litvak, M., Moore, D. J., Scott, R., and Torn, M.: The AmeriFlux network: A coalition of the willing, Agricultural and Forest Meteorology, 249, 444-456, 2018.

595 Pastorello, G., Trotta, C., Canfora, E., Chu, H., Christianson, D., Cheah, Y.-W., Poindexter, C., Chen, J., Elbashandy, A., and Humphrey, M.: The FLUXNET2015 dataset and the ONEFlux processing pipeline for eddy covariance data, Scientific data, 7, 1-27, 2020.

Quiring, S. M., Ford, T. W., Wang, J. K., Khong, A., Harris, E., Lindgren, T., Goldberg, D. W., and Li, Z.: The North American Soil Moisture Database: Development and Applications, Bulletin of the American Meteorological Society, 97, 1441-1459, 10.1175/bams-d-13-00263.1, 2016.

600 Reichle, R. H., De Lannoy, G. J., Liu, Q., Ardizzone, J. V., Colliander, A., Conaty, A., Crow, W., Jackson, T. J., Jones, L. A., and Kimball, J. S.: Assessment of the SMAP level-4 surface and root-zone soil moisture product using in situ measurements, Journal of hydrometeorology, 18, 2621-2645, 2017.

Reichstein, M., Falge, E., Baldocchi, D., Papale, D., Aubinet, M., Berbigier, P., Bernhofer, C., Buchmann, N., Gilmanov, T., and Granier, A.: On the separation of net ecosystem exchange into assimilation and ecosystem respiration: review and improved algorithm, Global change

605 biology, 11, 1424-1439, 2005.

Santanello Jr, J. A., Peters-Lidard, C. D., and Kumar, S. V.: Diagnosing the sensitivity of local land–atmosphere coupling via the soil moisture–boundary layer interaction, Journal of Hydrometeorology, 12, 766-786, 2011.

Santanello Jr, J. A., Peters-Lidard, C. D., Kumar, S. V., Alonge, C., and Tao, W.-K.: A modeling and observational framework for diagnosing local land–atmosphere coupling on diurnal time scales, Journal of Hydrometeorology, 10, 577-599, 2009.

610 Santanello Jr, J. A., Dirmeyer, P. A., Ferguson, C. R., Findell, K. L., Tawfik, A. B., Berg, A., Ek, M., Gentine, P., Guillod, B. P., and Van Heerwaarden, C.: Land–atmosphere interactions: The LoCo perspective, Bulletin of the American Meteorological Society, 99, 1253-1272, 2018.

Schumacher, D. L., Keune, J., Van Heerwaarden, C. C., Vilà-Guerau de Arellano, J., Teuling, A. J., and Miralles, D. G.: Amplification of mega-heatwaves through heat torrents fuelled by upwind drought, Nature Geoscience, 12, 712-717, 2019.

615 Seneviratne, S. I., Corti, T., Davin, E. L., Hirschi, M., Jaeger, E. B., Lehner, I., Orlowsky, B., and Teuling, A. J.: Investigating soil moisture–climate interactions in a changing climate: A review, Earth-Science Reviews, 99, 125-161, 2010.

Seneviratne, S. I., Wilhelm, M., Stanelle, T., van den Hurk, B., Hagemann, S., Berg, A., Cheruy, F., Higgins, M. E., Meier, A., Brovkin, V., Claussen, M., Ducharne, A., Dufresne, J.-L., Findell, K. L., Ghattas, J., Lawrence, D. M., Malyshev, S., Rummukainen, M., and Smith, B.: Impact of soil moisture-climate feedbacks on CMIP5 projections: First results from the GLACE-CMIP5 experiment, Geophysical Research

620 Letters, 40, 5212-5217, https://doi.org/10.1002/grl.50956, 2013.

Seo, E. and Dirmeyer, P. A.: Improving the ESA CCI Daily Soil Moisture Time Series with Physically Based Land Surface Model Datasets Using a Fourier Time-Filtering Method, Journal of Hydrometeorology, 23, 473-489, 10.1175/jhm-d-21-0120.1, 2022.

Seo, E., Lee, M.-I., and Reichle, R. H.: Assimilation of SMAP and ASCAT soil moisture retrievals into the JULES land surface model using the Local Ensemble Transform Kalman Filter, Remote Sensing of Environment, 253, 112222, 2021.

625 Seo, E., Lee, M.-I., Schubert, S. D., Koster, R. D., and Kang, H.-S.: Investigation of the 2016 Eurasia heat wave as an event of the recent warming, Environmental Research Letters, 15, 114018, 2020.

Seo, E., Lee, M.-I., Jeong, J.-H., Koster, R. D., Schubert, S. D., Kim, H.-M., Kim, D., Kang, H.-S., Kim, H.-K., and MacLachlan, C.: Impact of soil moisture initialization on boreal summer subseasonal forecasts: mid-latitude surface air temperature and heat wave events, Climate Dynamics, 52, 1695-1709, 2019.

630 Stommel, H.: Entrainment of air into a cumulus cloud, J. Meteor, 4, 91-94, 1947.

Tawfik, A. B. and Dirmeyer, P. A.: A process-based framework for quantifying the atmospheric preconditioning of surface-triggered convection, Geophysical Research Letters, 41, 173-178, 2014.

Tawfik, A. B., Dirmeyer, P. A., and Santanello, J. A.: The heated condensation framework. Part I: Description and Southern Great Plains case study, Journal of Hydrometeorology, 16, 1929-1945, 2015a.

635 Tawfik, A. B., Dirmeyer, P. A., and Santanello Jr, J. A.: The heated condensation framework. Part II: Climatological behavior of convective initiation and land–atmosphere coupling over the conterminous United States, Journal of Hydrometeorology, 16, 1946-1961, 2015b.

Tramontana, G., Jung, M., Schwalm, C. R., Ichii, K., Camps-Valls, G., Ráduly, B., Reichstein, M., Arain, M. A., Cescatti, A., and Kiely, G.: Predicting carbon dioxide and energy fluxes across global FLUXNET sites with regression algorithms, Biogeosciences, 13, 4291-4313, 2016.

640 Van de Boer, A., Moene, A., Graf, A., Schüttemeyer, D., and Simmer, C.: Detection of entrainment influences on surface-layer measurements and extension of Monin–Obukhov similarity theory, Boundary-layer meteorology, 152, 19-44, 2014.

Van den Hurk, B., Kim, H., Krinner, G., Seneviratne, S. I., Derksen, C., Oki, T., Douville, H., Colin, J., Ducharne, A., and Cheruy, F.: LS3MIP (v1. 0) contribution to CMIP6: the Land Surface, Snow and Soil moisture Model Intercomparison Project–aims, setup and expected outcome, Geoscientific Model Development, 9, 2809-2832, 2016.

645 Wulfmeyer, V., Turner, D. D., Baker, B., Banta, R., Behrendt, A., Bonin, T., Brewer, W. A., Buban, M., Choukulkar, A., Dumas, E., Hardesty, R. M., Heus, T., Ingwersen, J., Lange, D., Lee, T. R., Metzendorf, S., Muppa, S. K., Meyers, T., Newsom, R., Osman, M., Raasch, S., Santanello, J., Senff, C., Späth, F., Wagner, T., and Weckwerth, T.: A New Research Approach for Observing and Characterizing Land–Atmosphere Feedback, Bulletin of the American Meteorological Society, 99, 1639-1667, 10.1175/bams-d-17-0009.1, 2018.

Xue, Y., De Sales, F., Lau, W. K.-M., Boone, A., Kim, K.-M., Mechoso, C. R., Wang, G., Kucharski, F., Schiro, K., and Hosaka, M.: West
650 African monsoon decadal variability and surface-related forcings: second West African Monsoon Modeling and Evaluation Project Experiment (WAMME II), Climate dynamics, 47, 3517-3545, 2016.

Xue, Y., Yao, T., Boone, A. A., Diallo, I., Liu, Y., Zeng, X., Lau, W. K., Sugimoto, S., Tang, Q., and Pan, X.: Impact of initialized land surface temperature and snowpack on subseasonal to seasonal prediction project, phase i (ls4p-i): organization and experimental design, Geoscientific Model Development, 14, 4465-4494, 2021.

655 Zhang, Y., Wang, L., Santanello Jr, J. A., Pan, Z., Gao, Z., and Li, D.: Aircraft observed diurnal variations of the planetary boundary layer under heat waves, Atmospheric Research, 235, 104801, 2020.

Zreda, M., Desilets, D., Ferré, T., and Scott, R. L.: Measuring soil moisture content non-invasively at intermediate spatial scale using cosmic-ray neutrons, Geophysical research letters, 35, 2008.

660
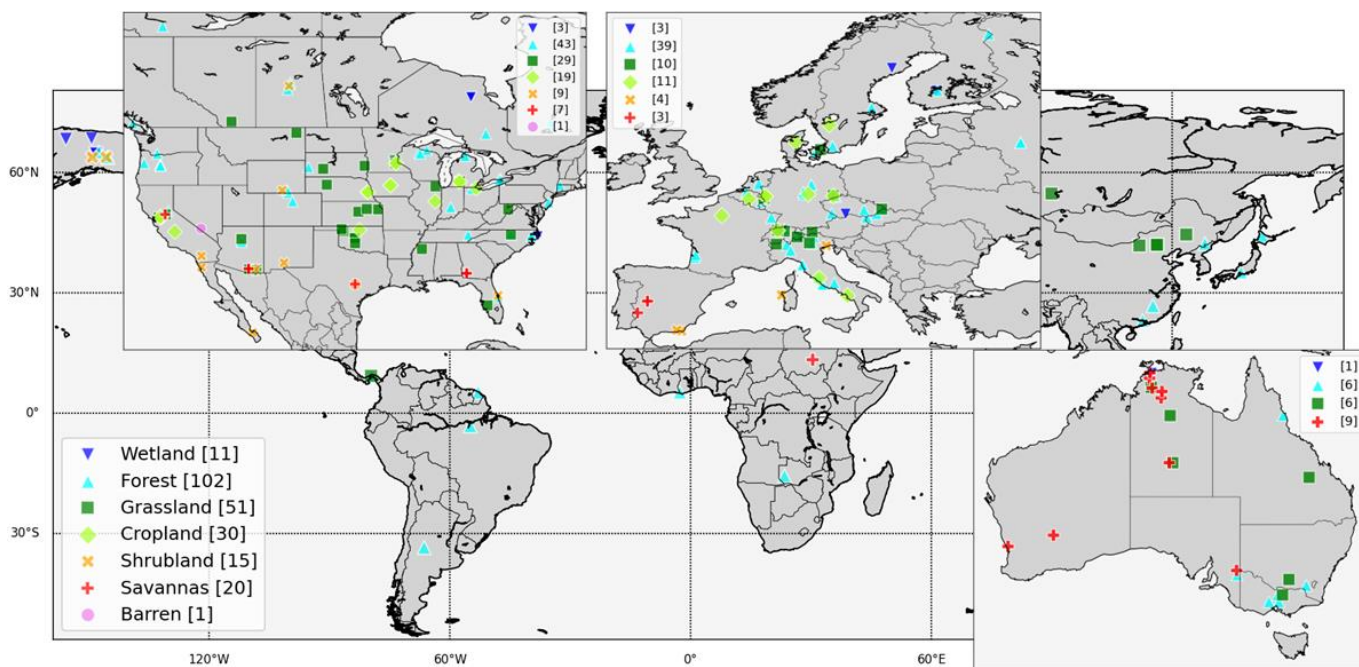
665

Figure 1: Locations of flux sites marked according to reported IGBP land cover. The bracketed numbers indicate the number of sites reporting each corresponding land cover.

670
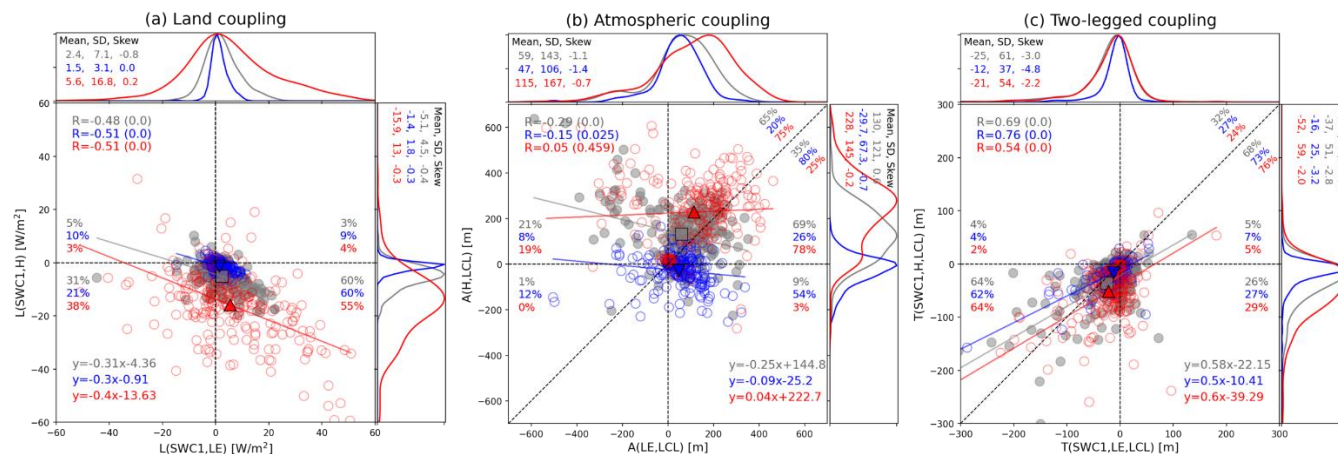
Figure 2: Scatter plot of (a) land coupling, (b) atmospheric coupling, and (c) two-legged coupling for daily (grey), midday averaged (11–13 LST; red) and midnight averaged (23–01 LST; blue) values at 230 flux sites. Regression lines are displayed in matching colours with the function given in the bottom of each panel. Squares, upward triangles, and downward triangles indicate the mean across 230 sites for daily, midday, and midnight, respectively. Correlations and corresponding p-values (bracketed) are denoted in the upper-left corners. On each scatter diagram, percentages of stations in each quadrant are indicated for daily, midday, and midnight data with corresponding colours. For the atmospheric and two-legged couplings, percentages are also indicated on either side of the diagonal (x=y) line. The distribution of the kernel density estimations corresponding to x- and y-axis is shown as marginal distributions along the upper and right sides of each scatter plot. Each is normalized to have the same maximum value; the mean, standard deviation, and skewness for each distribution are also shown.
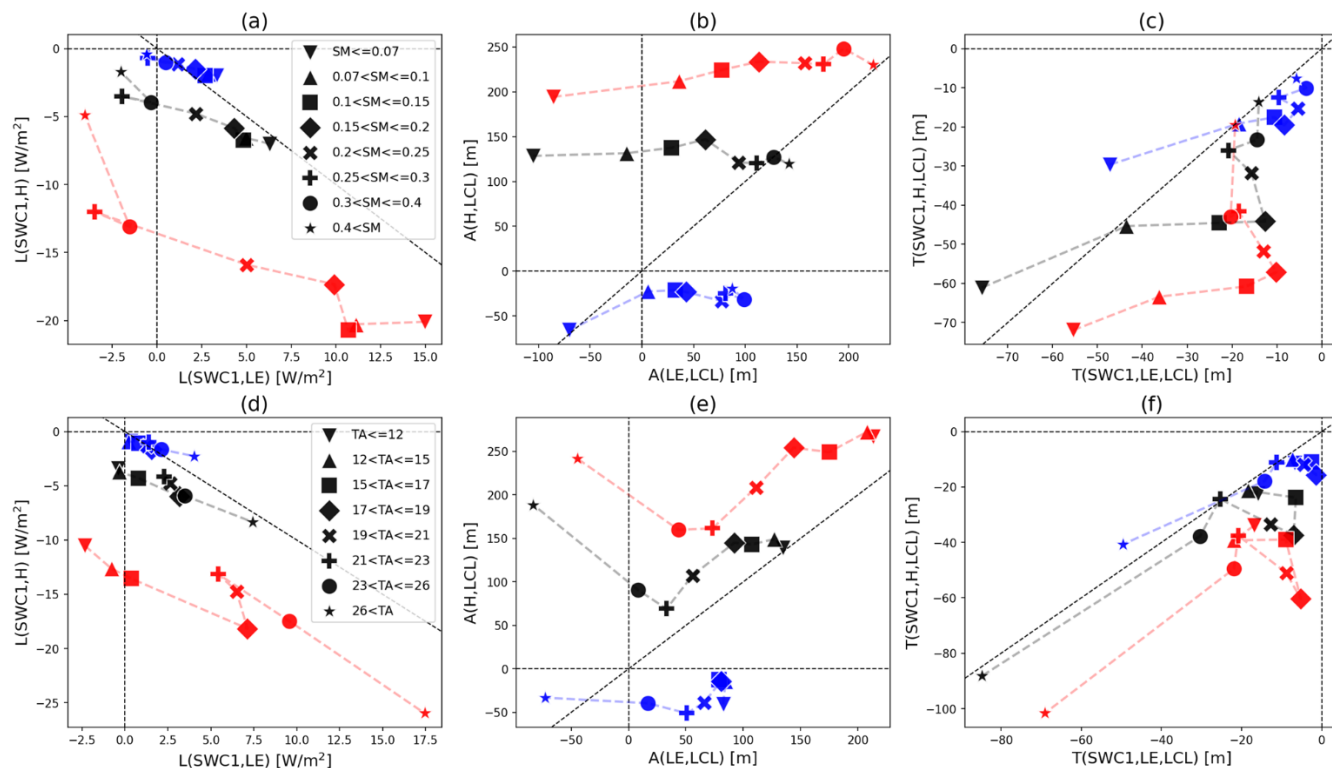
Figure 3: Scatter plots between moisture (x-axes) and energy (y-axes) pathway couplings for (a, d) land, (b, e) atmospheric, and (c, f) two-legged coupling for daily mean (black), midday mean (11–13 LST; red) and midnight mean (23–01 LST; blue), composited by surface soil moisture (upper row) and surface air temperature (bottom row) ranges indicated by symbols in the legends. Ranges are chosen so that each category has a similar sample size. Values in adjacent ranges are connected by dashed lines.
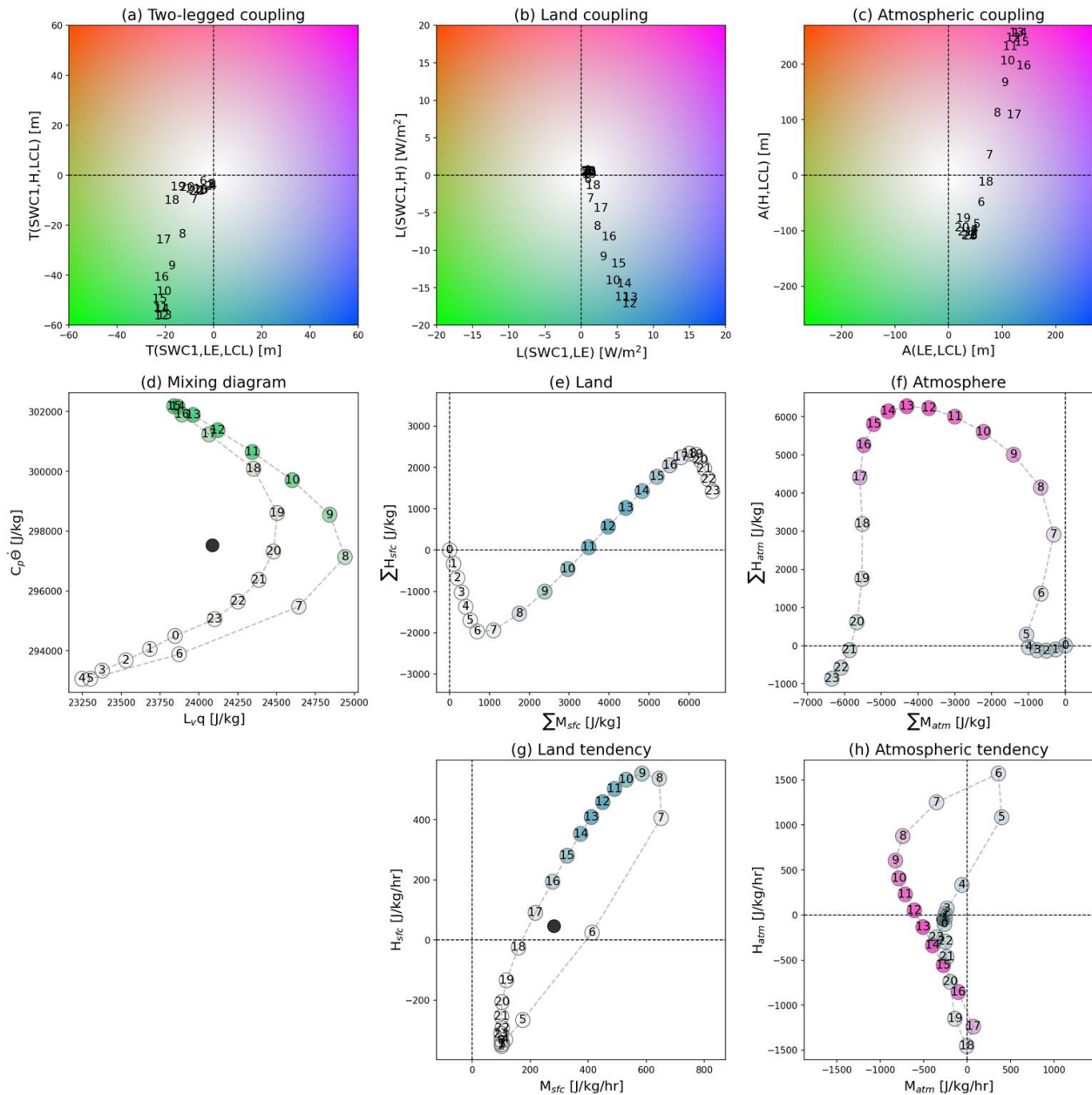
Figure 4: Scatter plot of hourly (a) two-legged, (b) land, and (c) atmospheric couplings composed to LE- (x-axis) and H- (y-axis)
690 **relevant term in which the numbers indicate local hour. Shaded colours depend on the sign of LE- and H-related couplings such as green (LE[-], H[-]), blue (LE[+], H[-]), red (LE[-], H^{+}), and purple (LE[+], H^{+}), and colour saturation denotes the coupling strength. (d) The hourly mixing diagram plots moist (x-axis) and heat (y-axis) energy content per unit mass within the mixed layer. The circles are shaded by the colour determined by two-legged couplings in (a) corresponded to the local hour. The black circle is the mean of the 24-hourly values. (e) The land and (f) atmospheric components of diurnal mixing diagram, which represents the**
695 **accumulated budgets relative to their corresponding vectors across the entire day, are shaded by land and atmospheric couplings, respectively. (g) The hourly land and (h) atmospheric vector representing their tendencies of the moist and heat energy budgets and the circles are shaded by corresponding couplings. In (g) and (h), the number represents the start of the hour over which tendencies are calculated.**
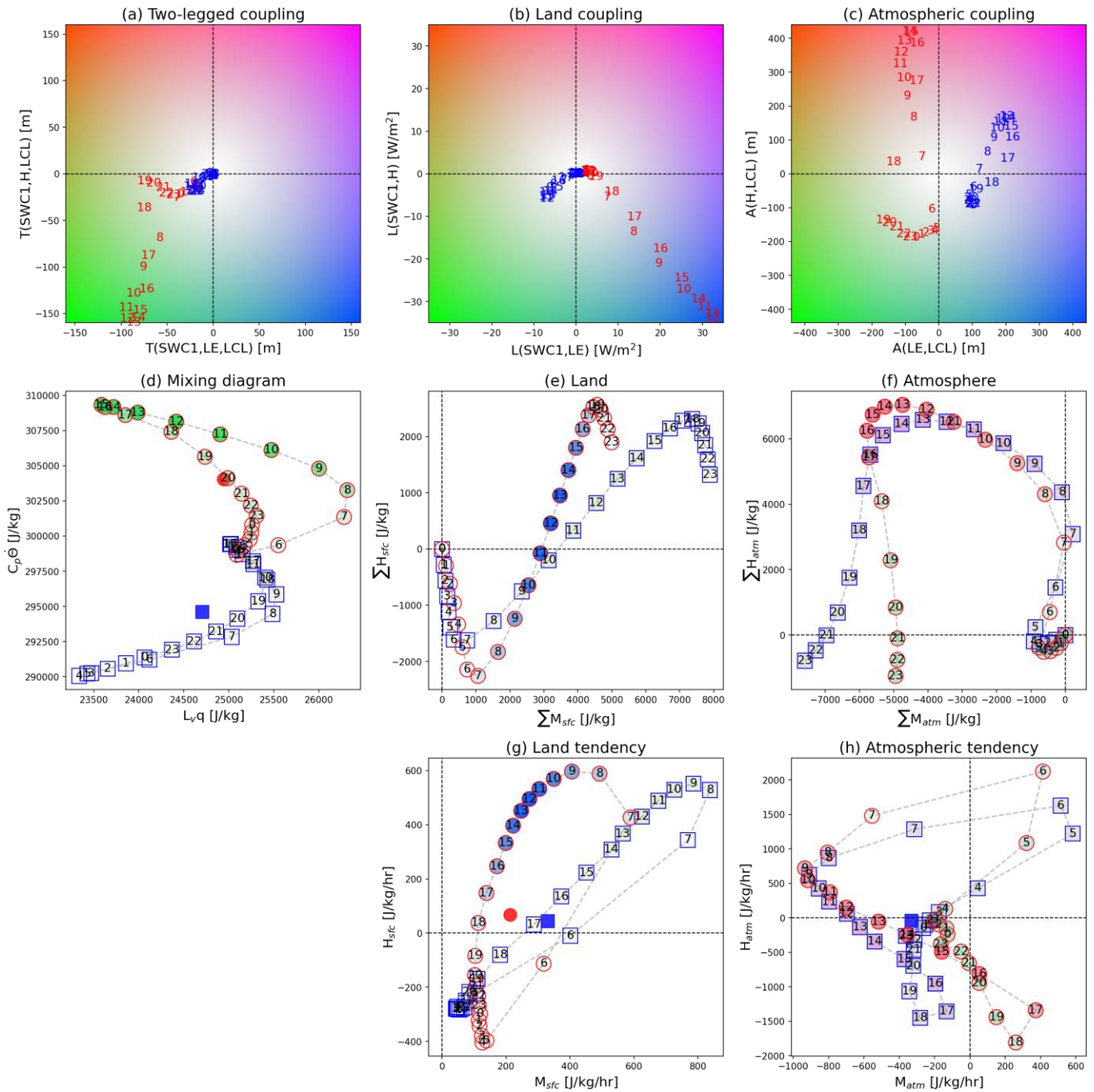
Figure 5: Same as Fig. 4, but for the sensitivity of water- (circles outlined in red) and energy- (squares outlined in blue) limited processes by the regime separation sampled by upper and lower 10% sites (N=23) described in section 3.3.